

# Influence of clustered defects on the fatigue performance of IN100

A. K. Matpadi Raghavendra<sup>1,2</sup>, L. Lacourt<sup>1</sup>, V. Maurel<sup>1</sup>, L. Marcin<sup>2</sup>, H. Proudhon<sup>1</sup>

<sup>1</sup>Centre des Matériaux, Mines Paristech, France

<sup>2</sup>Safran Aircraft Engines – Safran group, Etablissement de Villaroche, France

**Résumé** — The role of clustered defects on the fatigue performance of IN100 is discussed in this paper. Samples were experimentally tested and also numerically simulated. The numerical samples were modelled via image-based finite element modelling techniques through X-ray Computed Tomography. The characteristics of the defects are exploited via the tomographic scans. Furthermore, the possibilities of developing synthetic microstructure with the aid of spatial pattern analysis and deep neural networks are explained in this article.

**Mots clefs** — Ni-based superalloys, HCF, XCT, Spatial pattern analysis, GAN, Image-based FE model.

## 1. Introduction

The material Inconel 100 belongs to the Nickel based superalloy family and has its major use in the aviation industry, particularly for turbine discs or blade. However, many defects can be introduced during the casting of the material such as, shrinkages, pores, micro-voids, oxide films etc. These defects are known to degrade the High Cycle Fatigue (HCF) performance of the material. The pores are usually spherical in shape and are formed due to trapped gases or air bubbles while shrinkage driven cavities are caused due to the contraction of molten metal during freezing.

With the aid of non-destructive methods, it is possible to develop an image based finite element (FE) model that includes the real defects using X-ray Computed Tomography (X-ray CT). This method has shown excellent performance in the past [1]. But, developing and calibrating a model to describe the HCF performance remains a challenging task. However, many models have been developed to take into account as many conditions as possible. The LEFM theory works well on long cracks although fails to apply on short cracks. For long-cracks, the crack propagation threshold can be used to estimate the fatigue limit and has been used by several authors. However, LEFM assumes that the fatigue failure is due to one large defect.

A more simpler model is the Taylor's model. The model states that the fatigue life of a material reduces as much as the stress concentration factor (SCF) from its nominal value in the presence of macrostructural defects or stress concentrating features like notches [2]. The model has been used on other materials and has shown great results. Therefore, this work uses this model to predict the fatigue life of IN100 specimens. Furthermore, IN100 is known to exhibit viscoplastic behavior at high temperatures and therefore, numerical models are simulated under elasto-viscoplastic behavior law. The results from this strategy is compared with experimental results.

The mechanics of clustered defects is not straightforward as multiple parameters influence the initiation of crack and fatigue performance. However, the sensitivity of these parameters could be exploited in a probabilistic fashion by means of machine learning algorithms. Machine learning algorithms requires a large dataset for a robust training and therefore, in the context of fatigue testing with XCT inspection where the number of samples are limited, the use of synthetic samples that mimic the original samples is interesting. Via spatial pattern analysis, it is possible to distribute the defect volumes randomly within the samples such that it matches the randomness of the original samples [3, 4]. On the other hand, there exists a type of deep neural networks called generative adversarial network (GANs) which can learn the filters describing particular objects to generate a new, random object that

resembles the real objects. With the combination of these two strategies, synthetic samples of IN100 can be developed to finally create a large database.

## 2. Methods and procedures

### 2.1. Material and Experimental setup

Due to the high Ti/Al content (>11%), the two major phases present in IN100 are ordered  $\gamma'$  ( $\text{Ni}_3\text{Al}$ -type) phase embedded in a face-centered cubic (FCC) solid-solution  $\gamma$ -Ni matrix, See Table 1. Carbides and borides appear as minor phases. Material properties of IN100 depend on a number of interrelated microstructural parameters including the volume fraction of  $\gamma'$  to  $\gamma$ , grain size, elemental distribution, and precipitation of carbides and borides.

Table 1. Composition of Inconel 100

<i>Cobalt</i>	<i>Chromium</i>	<i>Aluminium</i>	<i>Titanium</i>	<i>Nickel</i>
15%	10%	5.5%	4.5%	Balanced

IN100 is a material mostly used as the turbine disk or blade in the aircraft engines. For the current work, four specimens are machined from casted bars. The grains are equiaxed with a size of 1.2mm and the only factor delimiting the fatigue life are the defect cavities. The specimens were 40 mm long with a gauge section diameter of 3.7 mm. To test the material under High Cycle Fatigue (HCF) regime, sinusoidal cyclic loads with a load ratio  $R=0$  and a frequency of 80 Hz were applied until a maximum of  $2 \times 10^6$  cycles at a temperature of  $750^\circ\text{C}$ . The specimens were tested using a MTS servo hydraulic machine. Apart from the four samples, samples with no macroscopic defects were prepared and tested under the same conditions to define the Wöhler curve for a healthy sample. The fatigue life of all the other four test samples are computed with respect to the healthy sample by fatigue reduction factor and is called as Debit in this article. Debit can be defined as the amplifying factor of stress by the presence of defects, which conversely diminishes the fatigue limit and is given by,

(1)

$$Debit = \frac{\sigma_{alt,healthy} | @ N \text{ cycles}}{\sigma_{alt,sample} | @ N \text{ cycles}}$$

Where  $\sigma_{alt,healthy}$  is the fatigue life of healthy samples at N cycles and  $\sigma_{alt,sample}$  is the fatigue life of test samples.

### 2.2. X-ray CT and Numerical methods

The test samples were characterized by XCT Nikon XT H 450 set up for a voxel size of  $25 \mu\text{m}^3$ . The image slices thus obtained were rendered into a volume. The images were treated and segmented using ImageJ software. After the segmentation, the volumes of defects were labelled separately and the surface meshes were extracted. The surface meshes were then inserted into the test sample and were registered in their actual positions, see Figure 1. The volume meshes are generated using ANSA software.

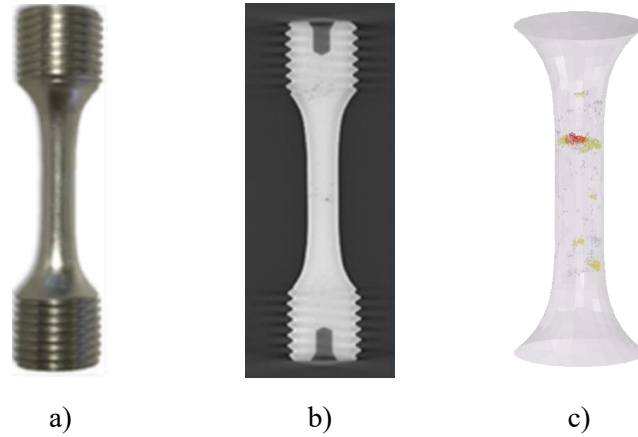


Figure 1. a) Test sample b) X-ray CT scan c) Image based FE model

The developed image based FE models are simulated numerically for one half cycle (tensile part of the cycle at a load ratio  $R = 0$ ) to compute the stress concentration factors (SCF) for ten largest defects of each test sample. In the current work, the failure criterion based on stress concentration is used and therefore it is important to consider the relaxation of stresses and also the evolution of local plasticity in highly stressed regions. So, an isotropic model with Kinematic hardening has been adopted to simulate the elasto-viscoplastic behavior of the material.

The hotspots are the local maximum stress values in the numerical model. To account for stress gradients close to local singularities, volumetric stress homogenization over a sphere with its center on the hotspot is performed. The radius for the stress homogenization are chosen in the range between 100-200 $\mu\text{m}$  such that they are in line with the theory of critical distances [5, 6].

The Taylor model, a criterion based on SCF is used to determine the fatigue limit of the test samples. According to this criterion, the SCF of the critical defect reduces the fatigue limit of the test samples from the materials nominal fatigue limit [2]. The model assumes the material will fail when the averaged stress over a critical volume surrounding the hot spot exceeds the nominal fatigue limit. In this work, the fatigue limit of healthy sample  $\sigma_{alt,healthy}$ , which is free of large defects and defect clusters would be the nominal fatigue limit. The critical defect of the sample is therefore the one with highest SCF after the Volumetric Stress Homogenization. And so, the criteria is given by

$$\sigma_D = \frac{\sigma_{D,healthy}}{K_{t,critical}}$$

2

Where,  $\sigma_D$  is the fatigue limit of the test sample or fatigue life at  $N$  number of cycles since the debit factor is assumed to be constant. In this criterion, SCF of critical defect  $K_{t,critical}$  is the debit factor that diminishes fatigue limit of the sample.

### 2.3. Generation of synthetic samples

Due to the complex responses of the clustered defects, machine learning algorithms are good candidates to estimate the sensitivity of various parameters of clustered defects (cluster size, morphological aspects, defect characteristics). Therefore, a large database of samples needs to be generated. The samples containing defects can be generated by means of spatial pattern analysis and the random morphology of the defects can be generated by means of Generative Adversarial Networks (GANs). In the current work, only the zone of clustered defects will be generated synthetically to

investigate the sensitivity of parameters influencing the fatigue properties.

### 2.3.1. Generative adversarial Network (GAN)

GANs are generative models using deep-learning methods. They are capable to comprehend and generate a new pattern which are similar to those of the dataset. Typically, GANs consist of two blocks, a generator and a discriminator as seen in Figure 2 and accepts a random noise vector to generate a data. The process involves training the discriminator separately with real data and then training the generator from the discriminator loss. By using the dataset of defects from tomographic scans, defect volumes of random morphologies and sizes are generated by applying the competencies of GAN [7].

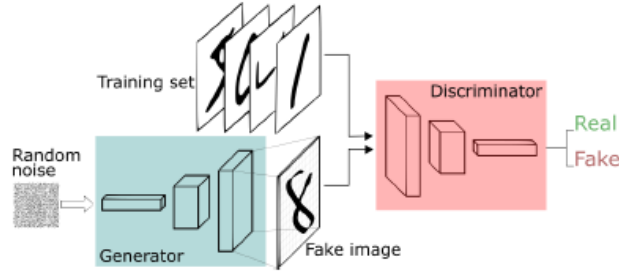


Figure 2. General architecture of GANs

### 2.3.2. Spatial Pattern Analysis

Spatial pattern analysis are vastly used in the field of astronomy, geography etc. However, the defects can be placed in their random locations after studying the patterns of the real samples. These random points can be generated by a simple homogenous Poisson process and is given by,

$$P\{N = k\} = \frac{\Lambda^k}{k!} e^{-\Lambda} \quad (3)$$

Where  $\Lambda$  is the intensity or density of number of points in region  $\mathbb{R}^3$  and  $k$  is the expected number of events. In the context of spatial randomness, three possible patterns can exist: 1) Complete spatial randomness 2) Clustered 3) Regular [4].

To analyze the patterns within the cluster, Ripley's K-function and Ripley's bivariate K-function were used. K-function is given by,

$$K(d) = \frac{V}{N} \sum_{i=1}^N \sum_{j \neq i}^N \frac{I(r_{ij} < d)}{N} \quad 4$$

Where  $I = 1$  if  $r_{ij} < d$  and zero otherwise.  $V$  is the volume of the region while  $N$  is the number of points. The method to compute K-function is as follows:

- i. Construct a circle around one arbitrary point ' $i$ ' of radius ' $d$ '.
- ii. Count the number of points that fall inside the circle.
- iii. Repeat the above steps for all points and sum the results.
- iv. Increase, the radius  $d$  and repeat the above process

The K-function tells the expected number of points within a radius  $d$  from any arbitrary point. For a pattern that follows homogenous poisson process, the K-function reduces to volume of

sphere with radius 'd' in 3D. If the K-function is larger than that of poisson process, the pattern is said to be clustered or else dispersed.

For this analysis, the centroids of the defect volumes were considered and the K-function was also iterated with respect to decreasing order of their size to estimate the size dependency in the cluster. The large defects did not show signs of clustering but upon considering the smaller defects, the curve deviates from the nominal poisson process and shows signs of clustering as seen in Figure 3.

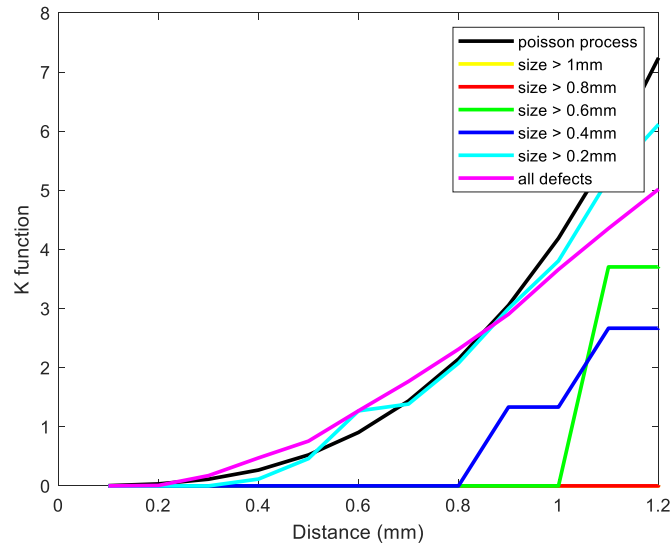


Figure 3. K-function for one of the samples with defects being considered in varying sizes

Figure 3 shows that the smaller defects less than sizes of 0.4 - 0.5mm are clustered. To estimate if these smaller defects are clustered among themselves or are clustered with the remaining larger defects, a bi-variate K-function was used. Bi-variate k-function is similar to Ripley's k-function but divides the data into two types and estimates the expected number of one type of points around the other type. Furthermore, it makes sense to consider the nearest distance between the surfaces of the defects rather than the centroidal distance to also include the shape factor in the analysis assuming that the shape shrinks to a point in an alternate plane.

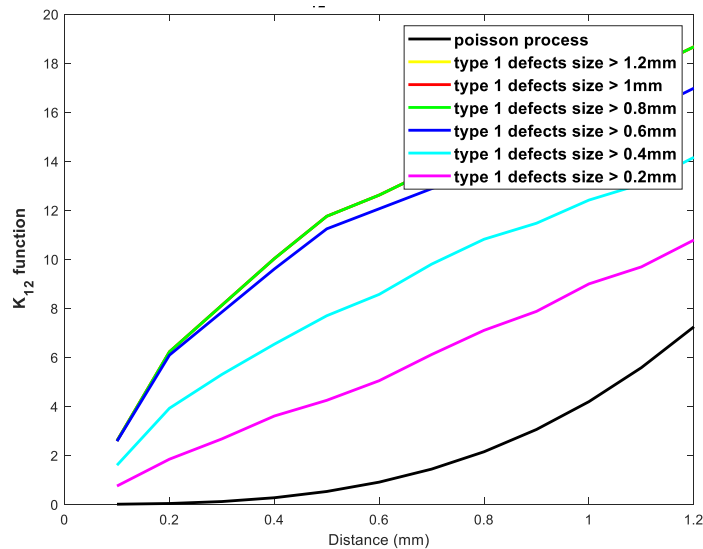


Figure 4. Bi-variate k-function with varying defect sizes for type 1 and the remainder as type 2

Figure 4 shows the expected number of type 2 defects within a distance from type 1 defects. It can

be seen that, the curves remains almost the same until defects of size 0.6 mm are considered for the type 1 but then drastically drops and therefore, the smaller defects (type 2 here) are found to be clustered with the larger defects (type 1). There exists a critical size above which the defects are randomly distributed while the defects below critical size are clustered with these large defects. This can be due to the resolution of X-ray CT where the parts of inter-dendritic shrinkages are broken or due to metallurgical process. Furthermore, a process similar to Voronoi tessellation and K-medoids algorithm was used to estimate the optimum number of clusters and the critical defect size which forms the center of these clusters. It was concluded that there are micro-clusters within the cluster volume of the samples as depicted in Figure 5a and therefore Neyman-Scott process was used to generate synthetic samples, as shown Figure 5.

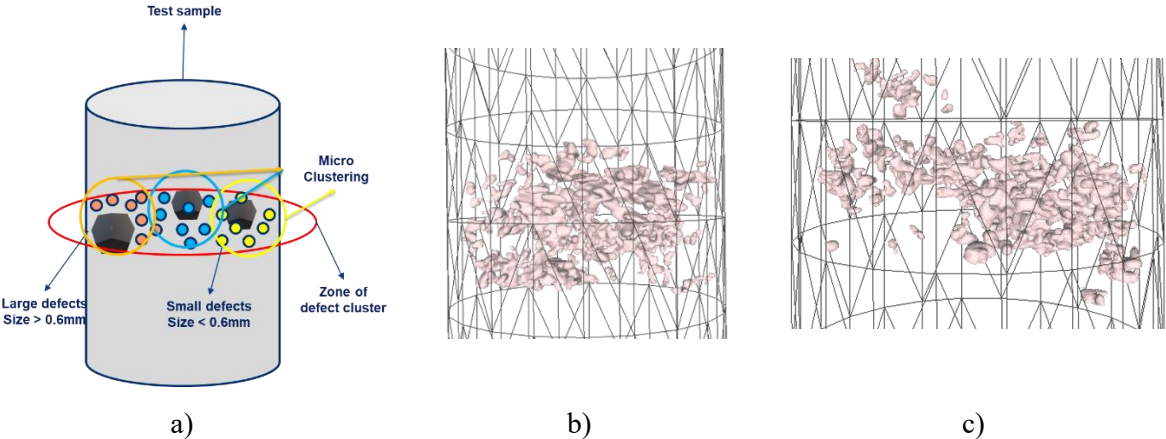


Figure 5 a) Illustration of micro-clustering within the defect clusters b) Synthetic sample c) Real sample

### 3. Results and discussions

The Wöhler curves for each sample is shown in Figure 6. To define the wöhler curves, 50% life probability curves from the industrial database is used. The database is created over thousands of tests carried out over the years. The stress amplitudes in the figure is normalized by the fatigue limit of healthy sample due to confidentiality reasons. A scanning electron microscopy analysis revealed the location of crack initiation and the defect that was responsible for the initiation, see Figure 7.

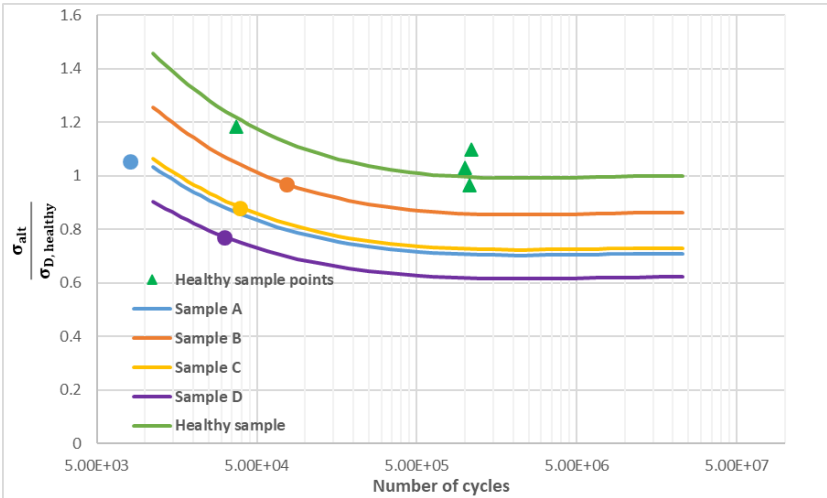


Figure 6. Wöhler curves for healthy and test samples as defined by debit factor. The tested samples are represented with markers of same colour for its respective wöhler curve. The cracks were found to initiate from one of the largest shrinkages. In some samples, the cracks

were found to propagate along the crystallographic plane towards the nearest shrinkage cavity during the early stage of crack propagation.

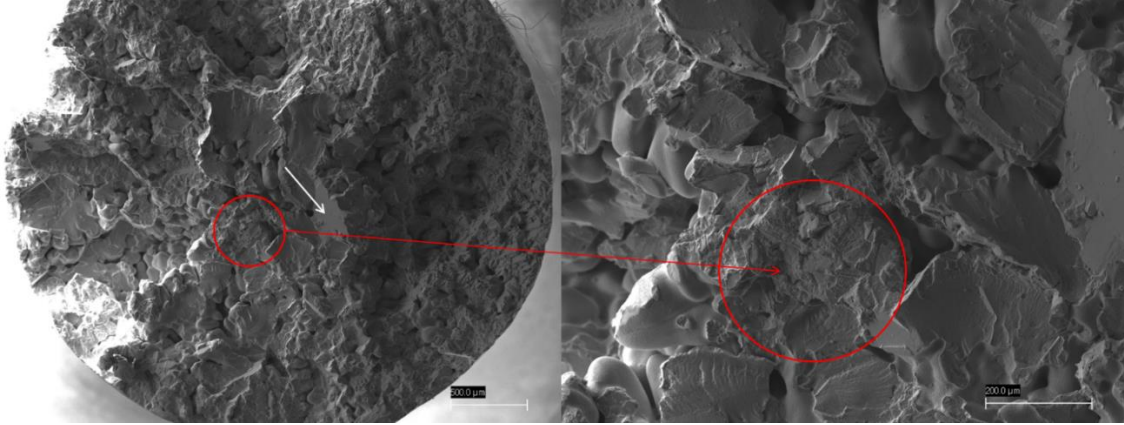


Figure 7. Crack initiation from the shrinkage cavity (image magnified on right) of sample B. The white arrow indicates the propagation of crack along the crystallographic plane.

Table 2. Comparison of experimental (exp) and numerical (num) results for test samples: The location of failure and the debit factor. Defect in red contour indicates the critical defect.

Sample A					Sample C				
<i>Failure plane Z- position (mm)</i>		<i>Debit</i>			<i>Failure plane Z- position (mm)</i>		<i>Debit</i>		
<i>Exp</i>	<i>Num</i>	<i>Exp</i>	<i>Num</i>	<i>Error (%)</i>	<i>Exp</i>	<i>Num</i>	<i>Exp</i>	<i>Num</i>	<i>Error (%)</i>
$\pm 0$	$\pm 0.5$	1.4	1.39	-0.3	$\pm 4$	$\pm 3.79$	1.35	1.52	12

Figure shows the porosity variation along the loading direction of the sample and also the fracture locations of the four test samples. All the test samples were found to fail in the region of clustered defects. With the aid of tomographic scans, the characteristics of the defects can be exploited and it has

been found that, the defects can be categorized into three types: 1) Shrinkages 2) Broken shrinkages and 3) pores. The broken shrinkages are part of the main inter-dendritic shrinkage but separated maybe due to the resolution of the tomographic scans or by metallurgical process and are typically closer to the large shrinkage with a broad range of aspect ratio and sphericity value between 0.3 and 0.6. The pores are usually spherical in shape while the shrinkages are torturous.

Through the numerical simulations, the debit factors (experimental debit and critical SCF) were compared to find the best radius of volumetric stress homogenization. The debit factors obtained numerically were found to be greatly coherent with the experimental results. The cracks are assumed to be initiating from the hotspot of the critical defect as also explained in the theory of critical distances and the location of these hotspots are in agreement with the plane of failure of the test samples. A brief synthesis of these results are shown in Table 2.

The mechanics of the clustered defects are found to be complex. Although, all the samples were found to be failing from a large shrinkage or a defect closer to surface, the presence of multiple large defect volumes in the cluster is found to deteriorate the fatigue life. Furthermore, in the presence of multiple large shrinkage of similar volumes and with similar distance from free surface, morphology seems to play a major role in the initiation of crack.

#### 4. References

- [1] Y. Hangai, O. Kuwazuru, T. Yano, T. Utsunomiya, Y. Murata, S. Kitahara, S. Bidhar and N. Yoshikawa, "Clustered Shrinkage Pores in Ill-Conditioned Aluminum Alloy Die Castings," *MATERIALS TRANSACTIONS*, vol. 51, no. 9, pp. 1574-1580, 2010.
- [2] D. Taylor, "Geometrical effects in fatigue: A unifying theoretical model," *International journal of fatigue*, pp. 413-420, 1999.
- [3] P. Wilson, "Inférence statistique de la population de défauts pour l'étude et la simulation de la fatigue oligocyclique d'un alliage d'aluminium de fonderie," *Ecole nationale supérieure d'arts et métiers - ENSAM*, 2017.
- [4] D. E. Khoukhi, N. Saintier, F. Morel, D. Bellett, P. Osmond and V.-D. Le, "Spatial point pattern methodology for the study of pores 3D patterning in two casting aluminium alloys," *Material characterization*, vol. 177, 2021.
- [5] D. Taylor, "The theory of critical distances," *Engineering Fracture Mechanics*, vol. 75, pp. 1696-1705, 2008.
- [6] D. Taylor, "Applications of the theory of critical distances in failure analysis," *Engineering Failure Analysis*, vol. 18, pp. 543-549, 2011.
- [7] J. G. Ian, P.-A. Jean, M. Mehdi, X. Bing, W.-F. David, O. Sherjil, C. Aaron and B. Yoshua, "Generative Adversarial Nets," *Advances in neural information processing systems*, vol. 27, 2014.